Characterization of hierarchically structured electrodes with different thicknesses by means of experiments and image analysis

Matthias Neumann[a,*], Amalia Wagner[b], Nicole Bohn[b], Markus Osenberg[c], André Hilger[c,d], Ingo Manke[d], Joachim R. Binder[b], Volker Schmidt[a]

[a] *Institute of Stochastics, Ulm University, Helmholtzstraße 18, D-89069 Ulm, Germany*
[b] *Institute for Applied Materials (IAM-ESS), Karlsruhe Institute of Technology, Hermann-von-Helmholtz-Platz 1, D-76344 Eggenstein-Leopoldshafen, Germany*
[c] *Department of Materials Science and Technology, TU Berlin, Hardenbergstr. 36, D-10623 Berlin, Germany*
[d] *Institute of Applied Materials, Helmholtz-Zentrum Berlin, Hahn-Meitner-Platz 1, D-14109 Berlin, Germany*

Abstract

Nano-structuring of active materials is a promising way to enhance the performance of Li-ion batteries regarding electronic properties, charge transfer during cycling as well as the resistance to mechanical stress. Moreover, producing thicker electrodes, i.e. thicker than 100 µm, leads to an increase in energy density of the cell and to a reduction of costs. In the present paper, thin and thick electrodes are compared, each manufactured with nano-structured and bulk active material, respectively. The focus is on their 3D microstructure, which is, in turn, important for the performance of the battery. Experimental approaches are combined with statistical image analysis based on synchrotron tomography. In general the results obtained by experiments are in good accordance with the ones obtained by image analysis. Moreover, image analysis allows for the computation of characteristics that are experimentally not accessible. In particular, the system of particle midpoints, the local volume fraction of active material at certain distances to the current collector foil, as well as the windedness and narrow constrictions of transportation pathways are analyzed using tools from spatial statistics and mathematical morphology. The main result is that the considered microstructure characteristics depend only slightly on the thickness of the electrode, while significant differences can be observed between electrodes manufactured with nano-structured and bulk active material.

Keywords: Lithium-ion batteries, electrode characterization, 3D imaging, statistical data analysis, process-microstructure-property relationships

1. Introduction

Lithium-ion batteries (LIBs) are one of the most promising key technologies nowadays [1] to get rid of fuel-based energy production and locomotion. Due to their high conversion efficiency, environmental-friendliness and their flexible use they are appropriate for both, mobile and stationary applications [2]. The hope is that going along with the elaboration of this technology allows us to further intensify the transition to renewable energy sources with LIBs being the main protagonist in electromobility. Important goals for nearby future concerning electromobility have already been

*Corresponding author. Phone: +49 731 50 23617. Email: matthias.neumann@uni-ulm.de.

determined but seem difficult to comply with up to now. Main causes are the acquisition costs for electric vehicles in comparison to the still lacking power and energy density, rate capability or long-term stability of LIBs, which are needed to be competitive to combustion engines.

Commercially available batteries for electric vehicles consist in principle of almost bulk active materials in order to achieve high energy densities. On the other hand, nano-structured active materials or nanocomposites are less common except for academic purposes, though they are showing clear advantages [3, 4] in comparison to their bulk counterparts. One of the advantages is their structural set-up, which can resist mechanical stress and crack formation caused by the de- and intercalation of Li^+-ions during electrochemical cycling. Furthermore, nano-structuring of active materials with nano-pores results in shorter ionic transport paths and an improvement of diffusion, which leads to better electronic properties and an enhancement of charge transfer during cycling. Thus, to improve energy and power densities of the cathode material, hierarchically structured composite electrodes can be pursued [5, 6, 7].

Moreover, higher electrode thicknesses in combination with the optimized cathode architecture are of interest since this leads to an increase in energy density of the cell unit due to the break down of kinetic limitations and most importantly to the lowering of battery-pack costs [8]. Nevertheless, increased coating thicknesses are going along with intensive caution in material processing and electrode preparation since induced inhomogeneities and defects affect the electrochemical behavior of the cell dramatically and limit the use of high electrode thicknesses [8]. A general description of these phenomena and their consequences can be found in [9], where the morphology of different types of electrodes used for LIBs is investigated based on 3D imaging.

In the present paper, we investigate the 3D morphology of electrode materials composed of two different active material powders, i.e. non-structured bulk and hierarchically-structured active material [4], by means of experiments and image analysis based on synchrotron tomography [10, 11]. For both cases we consider two composites varying in their thickness. Thereby, we analyze how the thickness influences the morphology of the composite, i.e. the electrode material. For this purpose, properties of the powders, like their particle size distributions, are investigated experimentally by laser diffraction and the obtained results are compared to results from image analysis. Moreover, using methods of mathematical morphology [12] and spatial statistics [13], structural characteristics of the electrodes are computed, which are not accessible experimentally as, e.g., the volume fraction of the percolating part of active part and the lengths of shortest paths through the active materials. In particular, we predict the so-called M-factor [14] of the active material, which is meaningful for the effective conductivity of the electrodes assuming that the additive material accumulates around the active material particles. The information obtained by such an investigation, where experiments, 3D imaging and statistical image analysis are combined, is helpful to get a better understanding of the relationship between parameters of the manufacturing process and the morphology of the electrode and thus the performance of LIBs, see also [15, 16]. In particular, the combination of experimental methods with statistical image analysis allows for a detailed investigation of the morphology of the electrode for a given set of manufacturing parameters.

The rest of this paper is organized as follows. To begin with, materials, 3D imaging and the pre-processing of image data are described in Section 2. Based on the pre-processed data, statistical image analysis is performed. The obtained results are discussed in Section 3, in comparison with experimental results. Section 4 concludes.

2. Materials and Imaging

2.1. Electrode preparation

For the comparison of electrodes with morphologically different lithium nickel cobalt manganese oxide particles and thicknesses, a dense pristine $Li(Ni_{1/3}Mn_{1/3}Co_{1/3})O_2$ powder (NM-3100, Toda America) with a mean aggregate particle size ($d_{50.0}$) of 6.7 µm and a BET surface of 0.35 m^2/g, called p-NCM, and a corresponding nano-structured powder (n-NCM) is used. The n-NCM powder is obtained by modifying the p-NCM powder in a process of grinding, spray drying and calcination. This results in an n-NCM powder with a mean particle size of 11.8 µm, a BET surface of 2.52 m^2/g and an internal porosity of 40.6 %. A more detailed description of powder processing and characterization can be found in [4]. The bulk densities of the two powders are measured by geometrical experiments in a measuring cylinder.

The electrodes are produced using p-NCM and n-NCM as active materials. Therefore, polyvinylidene difluoride (PVDF) binder (Solef 5130, Solvay Solexis), carbon black (Super C65, Imerys Graphite & Carbon), graphite (KS6L Imerys Graphite & Carbon) and the corresponding NCM powders are dispersed in N-methyl-2-pyrrolidone (Sigma Aldrich) using a vacuum equipped dissolver (VMA Getzmann) at 2000 rpm for 1 hour. The resulting slurries contained about 87 wt% NCM, 5 wt% graphite, 4 wt% carbon black and 4 wt% PVDF binder with a solid content of 21.9 vol% for p-NCM and 19.8 vol% for n-NCM. The electrode sheets are prepared by casting the slurries onto a 20 µm thick aluminum foil using a continuous laboratory coater (KTF-S, Mathis) equipped with doctor blade technology and convection dryer. By adjusting the gap of the doctor blade to 180 µm and 360 µm for the slurry with p-NCM, and to 190 µm and 370 µm for the slurry with n-NCM, an active material loading of approximately 12 mg/cm^2 and 24 mg/cm^2 in the electrodes is reached. Subsequently the as-prepared electrodes are called EL-12p, EL-24p, EL-12n, and EL-24n. After drying the layer heights of the electrodes are measured by a thickness gauge for the calculations of layer properties.

2.2. 3D Imaging

To examine the differences in electrode preparation caused by different active material powders and varying gap height during doctor blading, 3D imaging of these four electrode layers is performed. As a result we obtain 3D images, where the active material can be distinguished from the union of binder, additives, and pores. In the following, this union is called the binder-additives-pore phase (shortly: the bap-phase) as in [15].

2.2.1. Sample preparation

In order to optimize high-resolution tomography with synchrotron radiation for electrodes containing NCM active material, one needs to seize the field of view as the key parameter for sample preparation since it restricts the sample size. The high-resolution set-up visualized below in Figure 1 (a) provides a field of view of 1.75×1.17 mm^2. The p-NCM and the n-NCM electrodes are first inspected by means of optical microscopy to detect possible damages and to ensure that only the relevant parts of the samples are measured. The selected areas of the considered electrode foils with a size of 1.3×3 mm^2 are then cut out and stacked in pairs, using a stereo microscope, in order to increase the comparability of different samples. Finally, the sample stacks are fixed between acrylic rods, each of which is $1.5 \times 1.5 \times 10$ mm^3 in size as shown in Figure 1 (a).

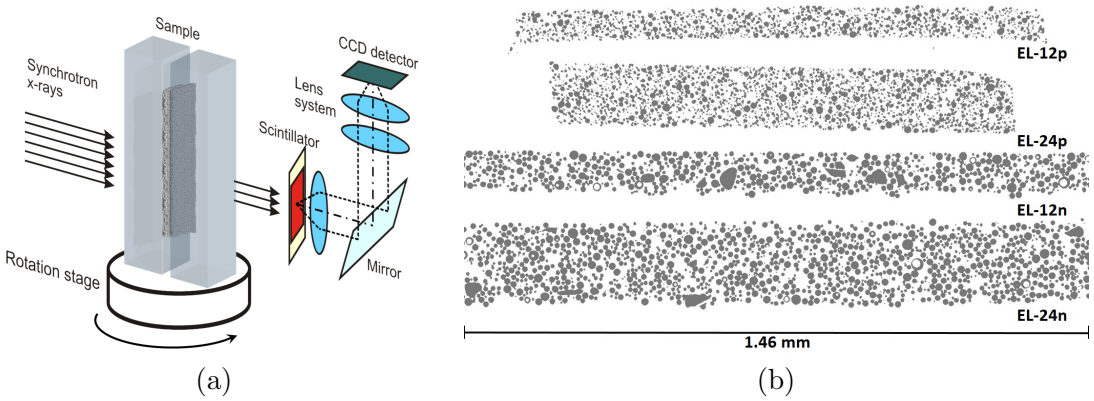

Figure 1: Schematic set-up of the BAMline synchrotron tomography station at BESSY II (a) and 2D slices of the binarized 3D images of electrodes EL-12p, EL-24p, EL-12n and EL-24n (b). Active material is represented in grey and the bap-phase in white.

2.2.2. Tomography

Synchrotron tomography measurements have been conducted at the BAMline at Bessy II in Berlin, Germany [17]. The tomography set-up and 2D slices of the binarized images are shown in Figure 1. The photons generated at a 7 Tesla wavelength shifter are monochromatized with a tungsten-silicon double multilayer monochromator X-ray optics. After transmitting the sample the monochromatic X-rays are partially transformed into visible light (emission maximum at 475 nm) using a 60 µm thick $CdWO_4$ scintillator. The optical set-up provided a 20 times magnification (Optique Peter) and the scintillator image is detected with a PCO.4000 camera (PCO AG) with a resolution of 4008 × 2672 pixels. The pixel size in combination with the 1.75 × 1.17 mm^2 field of view results in a final resolution of 0.438 µm per pixel. Due to the high absorption contrast of the materials of interest, phase contrast effects where not desired. Thus a 4 mm sample to scintillator distance is chosen. The sample thickness of up to 1.75 mm combined with the high absorption of the nano-porous NCM material of 21 cm^{-1} at 25 keV limits the selectable photon energy to a minimum of 20 keV. To ensure a transmission of over 12 %, we measure the sample at 25 keV. For each tomography, 2200 radiograms and 230 flatfields over an angular range of 180° are captured. Each image is exposed for 3 s resulting in a total measuring time of 2 h. A high precision rotary table with air bearings (Physik Instrumente) is used for the sample stage to reduce movement artefacts.

2.2.3. Pre-processing of image data

Based on the greyscale images, which we obtain as the output of synchrotron tomography, we assign each voxel either to the active material, to the electrode foil, or to the bap-phase. This allows for an investigation of the morphology of the electrodes. Moreover, for the analysis presented in Sections 3.2.1 and 3.2.2, the individual aggregate particles are extracted from 3D image data. For this purpose, we proceed as follows.

To begin with, the radiograms obtained from synchrotron tomography are normalized after subtraction of the detected background. A correlation-based algorithm is used to find the best fitting flatfield. After normalization, the radiograms are denoised with a total variation filter [18]. For each measurement, the filter parameters are set to half the standard deviation in a free beam area. The reconstruction is made using 'gridrec' [19], an implementation of the filtered back projection

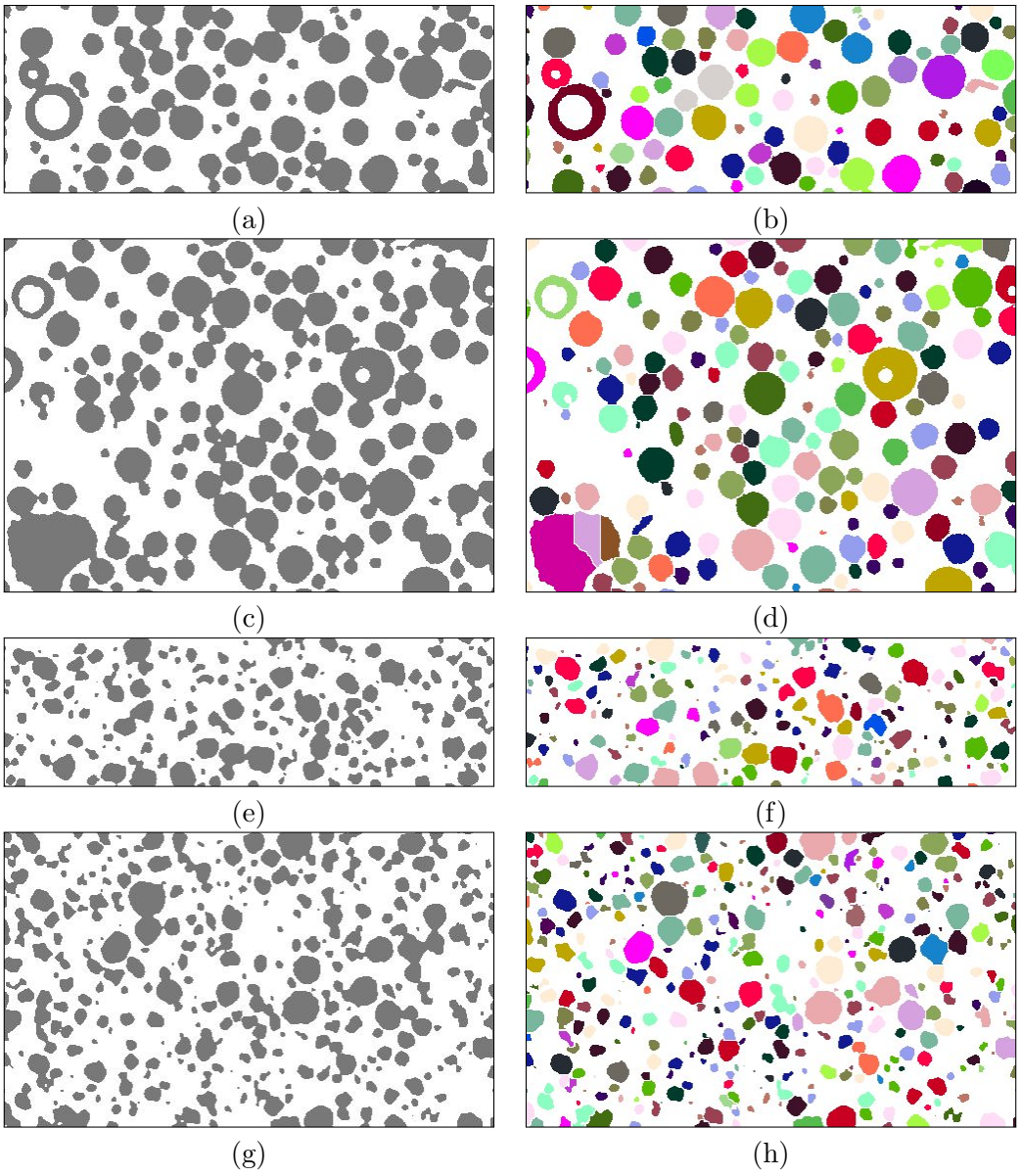

Figure 2: 2D cutouts for the samples EL-12n (a), EL-24n (c), EL-12p (e) and EL-24p (g) representing the active material and the bap-phase in grey and white, respectively. The length of the cutouts equals 220 µm, while the height corresponds to the thickness of the electrode. Correspondingly labeled images showing the extracted individual aggregate particles in different colors for EL-12n (b), EL-24n (d), EL-12p (f) and EL-24p (h). Note that the proposed algorithm for particle extraction is able to deal with those NCM particles exhibiting hollow spheres (b,d).

algorithm [20]. A non-local-means filter [21] is used for further noise reduction, where the so-called photometric distance parameter is also set to the standard variation of a sample free area. For the trinarization, i.e. to distinguish between NCM, the aluminum of the foil, and the bap-phase, we train a random forest classifier, which returns class-probability maps. In these maps, the probability of belonging to one of the three phases is stored for each voxel. For training and computing the class-probability map, the trainable Weka segmentation [22] is used, where feature reduction is

performed via Weka [23]. After the trinarization, the resulting data has to be cleaned further. Therefore, the resulting class-probability maps obtained from the classifier are hysteresis filtered resulting in three binary stacks for each class, respectively. Finally, those voxels of the aluminum class that are not connected to the aluminum foil have to be swapped to one of the other classes depending on their probability.

The reconstructed foil is used to straighten the electrodes as described in [16]. That is, the electrodes are transformed such that the foil is parallel to the xy-plane. In the following, we focus on the morphology of the NCM particles and the bap-phase. 2D slices of the reconstructions of synchrotron tomographs showing the NCM particles and the bap-phase are displayed in Figure 1. Based on the reconstructed electrodes after straightening, the individual aggregate particles are extracted from image data by the aid of the watershed algorithm. The watershed algorithm is a common tool in image analysis for object-based segmentation of image data. For an overview, we refer to [24, 25]. In our case it is challenging that a few aggregate particles in EL-12n and EL-24n exhibit the hollow spheres which occur in spray drying, seen in Figure 2 (a) and (c), which leads to problems with the watershed algorithm. These hollow spheres can not be closed by a simple cluster detection, since some of them are connected to the pore space between the particles. Thus, using the watershed algorithm, we detect spherical regions in the pore phase and add those regions to NCM. Finally these regions are re-assigned to the pore space again. For this purpose, we compute the watershed transform presented in [26] to partition the pore space into different regions. Then, each region with a sphericity larger than 0.8 is considered to be a hollow sphere of a particle. Note that sphericity is a characteristic taking values between 0 and 1 giving information, how spherical a particle is. If the sphericity of a particle equals 1, the particle is a perfect sphere. For a particle with volume V and surface area S, its sphericity ψ is formally defined by

$$\psi = \frac{1}{S}\sqrt[3]{36\pi V^2}, \tag{1}$$

see [27]. To estimate sphericity from image data, we estimate the volume of particles by counting voxels [13] and the surface area by the method described in [28]. Finally, the watershed algorithm of [26] is applied to the active material with closed holes and the holes are removed from the extracted individual aggregate particles afterwards. This procedure leads to an extraction of individual aggregate particles, which is visualized in Figure 2. Tiny regions with a volume equivalent radius of less than one voxel unit, i.e. 0.438 µm are considered as artifacts and are not taken into account for the statistical analysis of individual aggregate particles in Section 3.2.1. Besides that, one can observe in Figure 2 (b) and (d) that the algorithm is able to deal with the inner holes of aggregate particles. In general, the extraction of aggregate particles via the watershed algorithm coincides with how one would extract particles manually.

3. Results

3.1. Experimentally determined layer properties

The prepared electrodes vary in the morphology of the NCM powder and their loading densities according to the set gap height of the doctor blading tool. For EL-12p, a thickness, i.e. a dried layer height, of 75 µm with an active material loading of around 12 mg/cm^2 at a set gap height of 180 µm is reached. For EL-24p the thickness is 151 µm with an active material loading of 24 mg/cm^2 at a set gap height of 360 µm. By applying laser diffraction to the pure powders we

Table 1: Layer properties of the electrodes with p-NCM and n-NCM as active material.

electrode	EL-12p	EL-24p	EL-12n	EL-24n
powder	p-NCM	p-NCM	n-NCM	n-NCM
active material loading [mg/cm^2]	11.9 ± 0.1	24.6 ± 0.3	12.4 ± 0.1	23.4 ± 0.4
electrode thickness [µm]	75 ± 0.9	151 ± 1.5	101 ± 1.1	187 ± 3.0
volume fraction NCM [%]	34.2 ± 0.2	34.3 ± 0.1	25.6 ± 0.1	26.2 ± 0.4
volume fraction NCM including the internal porosity [%]	34.2 ± 0.2	34.3 ± 0.1	43.1 ± 0.2	44.1 ± 0.7
electrode porosity [%]	53.3 ± 0.3	53.1 ± 0.2	65.0 ± 0.2	64.2 ± 0.5
electrode porosity without internal porosity [%]	53.3 ± 0.3	53.1 ± 0.2	47.5 ± 0.3	46.3 ± 0.8
volume fraction binder, carbon black, graphite [%]	12.6 ± 0.1	12.6 ± 0.04	9.4 ± 0.1	9.6 ± 0.1

obtain mean aggregate particle sizes of 6.7 µm and 11.7 µm for p-NCM and n-NCM, respectively. Detailed information about characteristic layer properties of the four different types of electrodes are obtained by geometrical experiments. These calculations lead to electrode porosities of 53.3 % and 53.1 % for EL-12p and EL-24p, respectively. The volume fraction of NCM in the electrode layer amounts to 34.2 % for EL-12p and 34.3 % for EL-24p, respectively. Due to the internal porosity of the n-NCM powder in comparison to the p-NCM, the electrodes differ in their layer thicknesses. They are, despite of having nearly the same loading density and gap heights (190 µm/370 µm), higher than electrodes with p-NCM, namely 101 µm for EL-12n and 187 µm for EL-24n. Thus, the volume fractions of NCM account to 25.6 % and 26.2 % and the porosities of the electrode layers amount to 65.0 % and 64.2 %, which is about 10 % higher than for electrodes with p-NCM. However, the internal porosity of the n-NCM powder accounts to 40.6 % and if considered in the calculation, the volume fraction of NCM in the layers increases to 43.1 % and 44.1 %, respectively. Finally, the actual electrode porosities amount to 47.5 % for EL-12n and 46.3 % for EL-24n, which is slightly lower than for the electrodes with p-NCM. This results from the higher packing density of the n-NCM powder due to its particle morphology. Measurements of the bulk density result in 35.2 % for the p-NCM powder and 37.8 % for the n-NCM powder; which is in good agreement to former calculation with increased bulk densities for hierarchically structured composite electrodes. These and further properties of the four electrodes are summarized in Table 1.

3.2. Results of statistical image analysis

Based on the pre-processing of image data described in Section 2.2.3, we consider several cutouts of the four electrodes in the xy-plane (Figure 2). In z-direction, i.e., in the direction orthogonal to the xy-plane, the full thickness of the electrode is taken into account. In the xy-plane, the cutouts are of size 220 µm × 220 µm. While considering 30 cutouts for the electrodes EL-12n and EL-24n, we use 20 and 15 cutouts for image analysis of EL-12p and EL-24p, respectively, since the electrodes EL-12p and EL-24p are smaller, see Figure 1 (right). The representativeness of the cutouts is demonstrated in Section 3.2.3. In the following, all cutouts of the four electrodes are analyzed regarding properties of individual particles, the geometrical configuration of the point

pattern of particle centers and further system-oriented characteristics. Note that for this analysis the nano-pores within n-NCM particles are not taken into account as they are not visible in image data gained by synchrotron tomography.

3.2.1. Analysis of individual particles

To begin with, the probability density functions of volume equivalent radii and sphericities are estimated for individual aggregate particles, the morphology of which is thereby investigated. Throughout the present paper, the computation of probability density functions is performed via kernel density estimation [29].

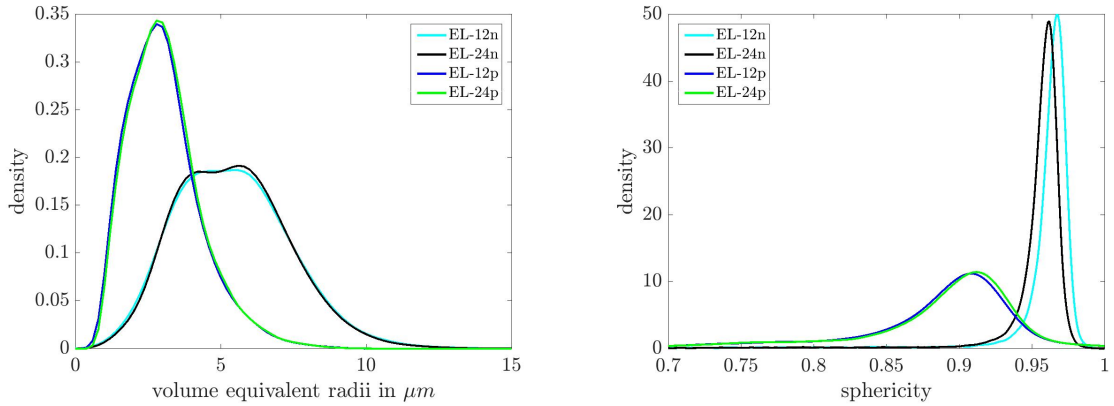

Figure 3: Probability density function of volume equivalent radii (a) and sphericity (b) of individual aggregate particles, both estimated from 3D image data.

Figure 3 shows that the particles in EL-12n and EL-24n are larger and more spherical than the particles in EL-12p and EL-24p, which can also be observed in the 2D images in Figure 2. These result are an indicator for a coarser microstructure – disregarding the effect of nanoporosity in n-NCM particles – of the electrodes manufactured with n-NCM. In Table 2 the 10%-, 50%- and 90%-quantiles, denoted by r_{10}, r_{50} and r_{90}, respectively, as well as mean values and standard deviations of the distributions of volume equivalent radii determined by image analysis are compared to the experimentally determined values for p-NCM and n-NCM powder, see Section 2.1. Even if the values obtained by image analysis slightly underestimate the experimentally determined values, a good qualitative agreement can be observed. Thus, we consider the extraction of aggregate particles from tomographic image data described in Section 2.2.3 as a valid basis for a further investigation of morphological differences between the four electrodes.

Moreover, in Figure 3 one can observe that the distribution of volume equivalent radii is wider for the electrodes manufactured with n-NCM in the sense that the peak of the probability distribution function lasts from about 4 µm to 6 µm. In particular, the standard deviation of the volume equivalent radius distribution is larger for the electrodes manufactured with n-NCM compared to those manufactured with p-NCM. Table 2 also shows the span φ of the particle size distribution defined by

$$\varphi = \frac{r_{90} - r_{10}}{r_{50}}, \tag{2}$$

which is a measure for the relative width of the particle size distribution, see [30]. All values of φ,

i.e. the ones determined by experiments and image analysis for both, p-NCM and n-NCM, are close to each other. In other words, no strong discrepancies regarding the relative width of the particle size distributions can be observed between p-NCM and n-NCM.

Table 2: Characteristics of the particle size distributions for p-NCM and n-NCM powder measured by laser diffraction as well as for particles extracted from 3D image data representing the four electrodes EL-12p, EL-24p, EL-12n and EL-24n.

	r_{10} [µm]	r_{50} [µm]	r_{90} [µm]	mean [µm]	standard deviation [µm]	span
p-NCM	2.18	3.35	5.15	3.54	1.18	0.89
EL-12p	1.58	2.91	4.73	3.06	1.27	1.08
EL-24p	1.63	2.96	4.78	3.12	1.27	1.06
n-NCM	3.34	5.88	9.05	6.08	2.22	0.97
EL-12n	3.07	5.31	7.93	5.42	1.95	0.92
EL-24n	3.10	5.32	7.89	5.42	1.92	0.90

3.2.2. Analysis of point patterns of particle centers

Besides the analysis of the distributions of particle sizes and sphericities, the extraction of individual aggregate particles allows us to compute their barycenters, which form three-dimensional point patterns within the electrodes. The morphologies of these point patterns reflect the structural changes of the ensemble of particles during casting. Furthermore, we investigate whether the geometry of the point pattern is influenced by the manufacturing of the electrodes itself, e.g. by the chosen gap height, and by the powder used as active material. The point patterns are analyzed with methods of spatial statistics, see e.g. [13, 31]. For this purpose, we determine the intensity, which is the mean number of points per unit volume, the nearest-neighbor distance distribution function, the pair-correlation function, and the mark-correlation function of these point patterns.

Table 3: Intensities of point patterns of particle midpoints.

	EL-12p	EL-24p	EL-12n	EL-24n
intensity$[10^{-3}\,\mu m^{-3}]$	1.7	1.6	0.5	0.5

The value $N(r)$ of the nearest-neighbor distance distribution function N at $r > 0$ is defined as the probability that the distance of an arbitrary barycenter to its nearest neighbor is smaller or equal than r. The pair-correlation function g quantifies interaction within a point pattern. If $g(r) = 1$ for each $r > 0$, then there is no interaction at all and we are in the situation of complete spatial randomness. On the other hand, for pairs of points having a distance r from each other, $g(r) > 1$ indicates clustering effects, while repulsion occurs if $g(r) < 1$. Besides exclusively considering the locations of particle midpoints, one can attach, e.g., the volume equivalent radii of the particles to their midpoints as marks. Then, the value $\mathrm{cor}(r)$ of the mark-correlation function cor at $r > 0$ is defined as the correlation coefficient of marks of two points which have distance r from each other. Note that the term mark-correlation function is defined in different ways in the literature [32]. The mark-correlation function considered in the present paper corresponds to the definition given in Equation (2.7) of [32].

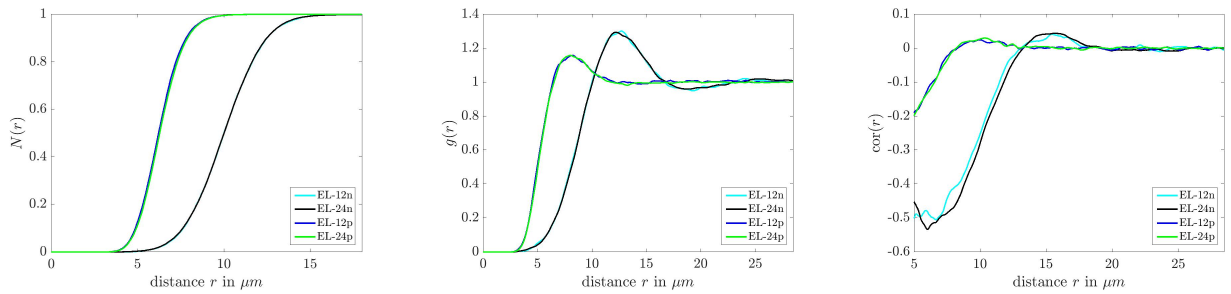

Figure 4: Nearest-neighbor distance distribution function (a), pair-correlation function (b) and mark-correlation function (c) for the point patterns of particle midpoints.

The computed results are presented in Table 3 and Figure 4, respectively. They reveal no differences for electrodes manufactured with the same powder. These results confirm once more that the particles in EL-12n and EL-24n are larger than in EL-12p and EL-24p, which implies a coarser electrode microstructure for electrodes manufactured with n-NCM provided that nanoporosity is not taken into account. In particular, the intensity of particle midpoints in the electrodes manufactured with p-NCM is with 0.0017 μm^{-3} and 0.0016 μm^{-3} three times larger than in electrodes manufactured with n-NCM (both 0.0005 μm^{-3}), i.e. in p-NCM electrodes there are three times more NCM particles per unit volume compared to n-NCM electrodes.

In the case of p-NCM, 99% of the nearest neighbor distances are between 3.1 µm and 9.9 µm, while in the case of n-NCM 99% of the nearest neighbor distances, see Figure 4(a), are between 5.1 µm and 15.4 µm. Moreover, note that the nearest neighbor distribution has a steeper increase for EL-12p and EL-24p than for EL-12n and EL-24n. This is in good accordance with the fact that the particle size distribution of n-NCM is broader than the one of p-NCM. In all point patterns, the pair-correlation function, see Figure 4(b), shows repulsion effects between pairs of points for small distances ($0-6.3$ µm in the p-NCM case and $0-10.1$ µm in the n-NCM case) followed by clustering effects ($6.3-11$ µm in the p-NCM case and $10.1-16.6$ µm in the n-NCM case), which are stronger for EL-12n and EL-24n. After small repulsion effects no further interaction can be observed for distances larger than 14 µm (p-NCM case) and 23 µm (n-NCM case). The general shape of the four estimated pair-correlation functions is typical for random sphere packings, the radii of which follow a continuous distribution [33, Figure 4]. Due to the packing of particles the positions of particle midpoints are spatially correlated, provided that the particles are sufficiently close. The computation of the pair-correlation functions allows us to quantify the range of this spatial correlation.

Considering the mark correlation function, presented in Figure 4(c), one can see that for pairs of points with small distances ($0-11.7$ µm in the p-NCM case and $0-15.0$ µm in the n-NCM case) the volume equivalent radii are negatively correlated. This means that particles, which are located close to each other, differ typically significantly in terms of their size. A further consequence of the presented analysis is that there is no interaction between pairs of points regarding their location and regarding their volume equivalent radii for distances larger than 11.7 µm for EL-12p and EL-24p as well as for distances larger than 23 µm for EL-12n and EL-24n. The shorter range of dependence in electrodes produced with p-NCM powder shows once more that these electrodes possess a finer microstructure than the ones produced with n-NCM powder due to the smaller particle sizes.

The main result of analyzing the point pattern of barycenters is that the varying gap height during casting does not affect the alignment of aggregate particles in the layer. This was not necessarily to be expected, because different processing parameters can affect the morphology, and thus the quality, of the electrode structure and segregation processes during casting can alter the arrangement of powder particles. Moreover, the analysis of the point patterns of particle midpoints reveals quantitative differences between the electrodes manufactured with p-NCM powder and n-NCM powder. Nevertheless, the point patterns are qualitatively similar in the sense that the functional characteristics shown in Figure 4 exhibit a similar shape.

3.2.3. Analysis of system-oriented characteristics

After the investigation of individual particles and the point pattern of particle midpoints, system-oriented characteristics are compared for the four electrodes to examine relationships between different powders and the morphology of the particle systems in the electrodes. At first, we investigate the volume fraction of the NCM-phase in dependence on the z-coordinate. The lower the z-coordinate, the lower is the distance to the aluminum foil. The results are represented in Figure 5, where the averages of local volume fractions are shown in red for each of the four electrodes. Note that the averages of local volume fractions correspond approximately to the experimentally determined values of the NCM volume fractions in Table 1. In general, no trend regarding volume fraction can be observed in dependence of the distance to the layer. Only at the region close to the aluminum foil, lower volume fractions are observed for all samples. The reason is that due to the high sphericity of aggregate particles, less space at the foil, i.e. at the boundary of the electrode, can be filled by active material. This effect is stronger for the thinner electrodes, i.e., more active material is located close to the foil in the thicker electrodes. In addition to the averaged local volume fractions, the local volume fraction computed for one single cutout is visualized in Figure 5. Here a periodic change in volume fraction becomes visible, which represents the layering of spherically-shaped particles. Note that the periodicity averages out, when considering all cutouts of the samples. Both effects, the periodicity as well as the local effects close to the foil are subsumed under the term 'wall effect' in the literature [34, 35], which is typical for sphere packings.

Next, we estimate transport relevant characteristics for each electrode, i.e. the volume fraction of the solid phase ε, its connectivity properties as well as its mean geodesic tortuosity τ and constrictivity β. For the computation of ε, we use the so-called point-count method [13] on the voxel grid, i.e., the number of voxels belonging to the solid phase is divided by the number of all voxels. As a quantification of connectivity properties of the electrode, we consider the fraction C of the solid phase which is connected to the bottom as well as to the top of the electrode. To identify connected components of the electrode structure from image data we use the algorithm presented in [36]. Mean geodesic tortuosity τ is defined as the ratio of the averaged shortest path length through the electrode over its thickness, while constrictivity β quantifies the strength of bottleneck effects. Note that τ is here a purely geometrically defined characteristic in contrary to concepts of effective tortuosities available in the literature [37]. Constrictivity has been introduced in [38] for complex microstructures via $\beta = r_{\text{min}}^2/r_{\text{max}}^2$. The value r_{max} is defined as the maximum radius, for which the value of the size distribution with respect to the spherical granulometry [12, 28] equals $\varepsilon/2$. Heuristically speaking, r_{max} is the maximum radius such that half of the active material phase can be covered by spheres of radius r_{max} being completely contained in the active materials phase. Furthermore, r_{min} can be considered as the radius of the characteristic bottleneck in the microstructure. By definition, β is between 0 and 1, where lower values indicate a stronger effect of bottlenecks. In the case $\beta = 1$ there are no bottlenecks at all. A mathematically rigorous definition

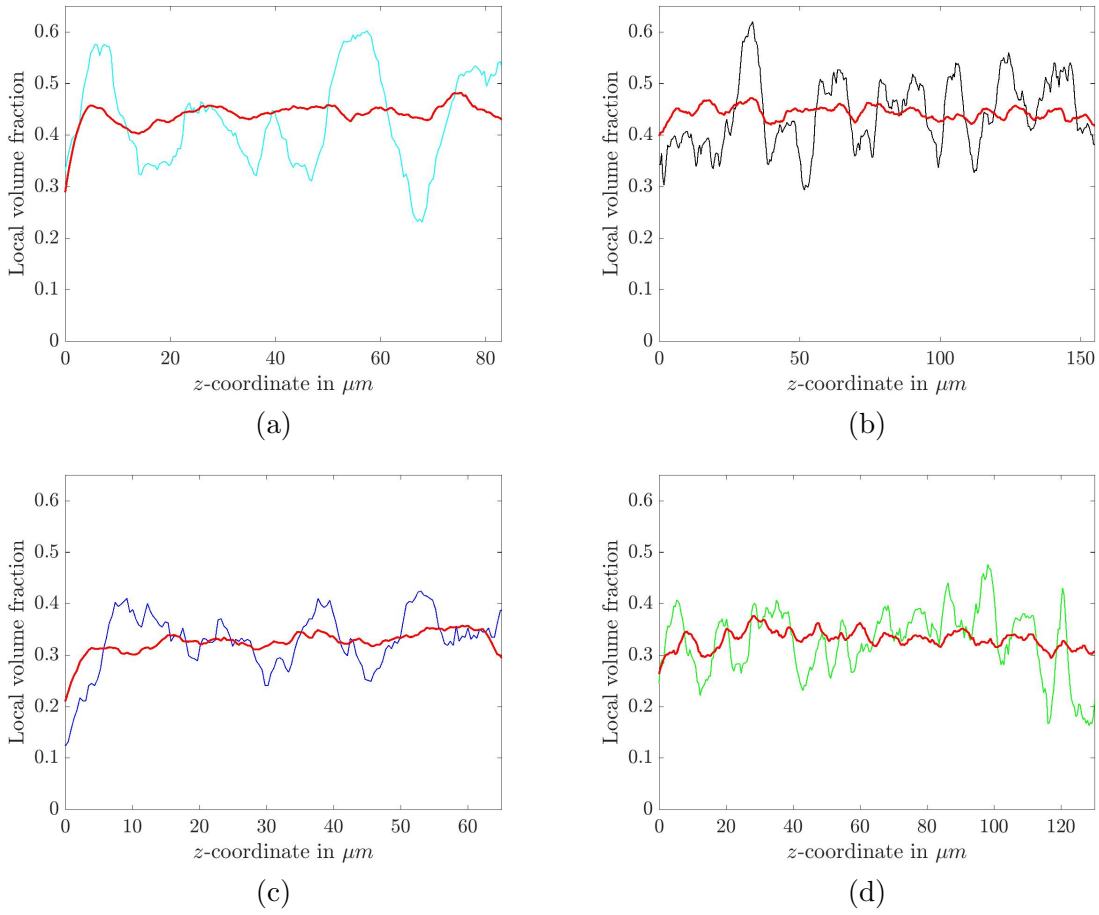

Figure 5: Local volume fractions of the samples EL-12n (a), EL-24n (b), EL-12p (c) and EL-24p (d). The average of local volume fractions over all cutouts are displayed in red. Additionally, a curve of showing the local volume fraction of a single cutout is visualized for each sample in cyan, black, blue and green, respectively.

Table 4: Transport relevant characteristics and their standard deviation with respect to the different cutouts.

	EL-12p	EL-24p	EL-12n	EL-24n
ε	0.326 ± 0.008	0.330 ± 0.004	0.442 ± 0.006	0.445 ± 0.005
τ	1.25 ± 0.02	1.22 ± 0.01	1.17 ± 0.01	1.14 ± 0.01
$r_{\min}[\mu m]$	0.98 ± 0.01	1.05 ± 0.07	1.57 ± 0.05	1.64 ± 0.07
$r_{\max}[\mu m]$	3.00 ± 0.06	3.03 ± 0.04	6.00 ± 0.09	5.93 ± 0.07
β	0.106 ± 0.004	0.120 ± 0.014	0.069 ± 0.006	0.077 ± 0.008
M-factor	0.044 ± 0.005	0.052 ± 0.003	0.073 ± 0.003	0.084 ± 0.004
C	0.967 ± 0.005	0.975 ± 0.002	0.991 ± 0.002	0.991 ± 0.001

in the framework of random sets is given in [39] for both, τ and β. Note that τ and β are computed for the percolating part of the solid phase determined with the Hoshen-Kopelman algorithm. In [14] the empirical formula

$$M = \frac{\varepsilon_{\text{eff}}^{1.15}\,\beta^{0.37}}{\tau^{4.39}} \tag{3}$$

has been derived by a combination of stochastic modeling and numerical simulations to predict the M-factor of a microstructure, which is the ratio of effective over intrinsic conductivity, where $\varepsilon_{\text{eff}} = C\varepsilon$. The formula has been validated with 3D image data of diverse real microstructures as, e.g., anode material of solid oxide fuel cells [14] and porous silica monoliths [40]. In our case we predict the M-factor of NCM in the prepared electrodes with this formula. Note that this predicted M-factor is not the same as the M-factor of the complete electrode, which also consists of additive materials, i.e. binder, carbon black and graphite. These additive materials contribute to the effective conductivity with a much larger intrinsic conductivity than NCM itself. Assuming that the additive material is accumulated around the NCM particles, mean geodesic tortuosity and constrictivity of the active material are also meaningful qualitative characteristics for the effective conductivity of the complete electrode, although quantitative relationships are not known so far. Under this assumption, electronic transport paths for example are shorter, if the transport paths through the active material are short.

The results are given in Table 4. First of all, note that the standard deviations of all considered characteristics regarding the different cutouts are small, such that the chosen cutouts can be considered as representative. The volume fraction of EL-12n and EL-24n is with 44% about 12% larger than the volume fractions of EL-12p and EL-24p, which agrees well with the values in Table 1. These results show that the particles in electrodes manufactured with n-NCM are tighter packed. This is in good accordance with the shorter pathways through the electrodes EL-12n and EL-24n compared to the electrodes EL-12p and EL-24p. The volume fractions estimated from 3D image data are in good accordance with the experimentally determined ones (Section 3.1). Moreover, it is remarkable that the value of C is close to 1 for all four electrodes despite of volume fractions below 50 %. Due to larger particles of n-NCM, $r_{\min}$ and $r_{\max}$ are larger in the n-NCM case than in the p-NCM case. However, the proportion of $r_{\min}$ and $r_{\max}$ is different and we observe lower values of constrictivity for EL-12n and EL-24n. A possible reason for that is the higher standard deviation of particle sizes in EL-12n and EL-24n compared to EL-12p and EL-24p. This is in good accordance with [41], where the constrictivity in systems of random tubes is systematically varied by the standard deviation of the size of the tubes. More precisely, larger standard deviations lead

to lower values of constrictivity.

For both powders, the shortest path lengths are longer and the values of constrictivity are smaller for the thin electrodes. Note that τ is – as the percolation threshold [42, Chapters 9 and 10] – a morphological descriptor for the connectivity of the system of NCM-particles. Thus, the reason for lower values of τ in thinner electrodes might be that, for similar microstructures, the percolation threshold is typically the larger the thinner the microstructure is, as it has been observed in [43, 44]. The higher values of constrictivity for the thicker electrodes might be explained by the fact that there exist more possible pathways for intruding spheres to fill the NCM-phase the thicker the microstructure is. Then, it is more likely that an intrusion of larger spheres (compared to the thinner electrodes) can fill 50 % of the NCM-phase. This hypothesis is supported by the computed values of $r_{\min}$, which are larger for EL-24n and EL-24p compared to EL-12n and EL-12p, respectively. These interpretations regarding the relationships between the thickness of the electrodes and the values of τ and β are only reasonable in the case that only the thickness of the electrode is varied since τ and β do not only depend on the percolation of transport paths, but also on their quality, i.e. their length and width.

The predicted values of M-factors corresponding to EL-12n and EL-24n are higher than the ones of EL-12p and EL-24p. This means that the ensemble of NCM particles exhibits better transport paths for the hierarchically structured materials provided that the nanoporosity, which is not visible in synchrotron images, is not taken into account. These findings correlate very well with the reduced internal resistances of lithium ion battery cells when using nanostructured NCM materials [4].

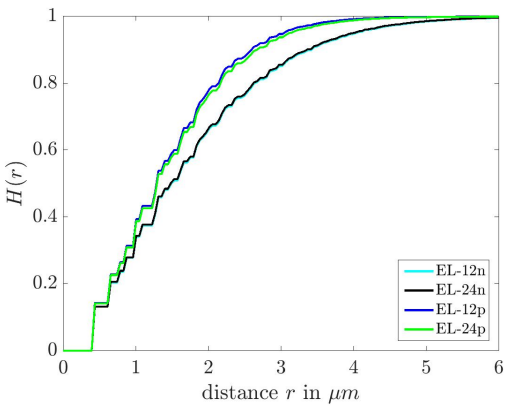

Figure 6: Mean spherical contact distance distribution function for the considered electrodes. Distances from pores to NCM are considered.

Furthermore, we consider the spherical contact distribution function H_s, which is a distributional characteristic of random spatial structures [13]. The value $H_s(r)$ is defined as the probability that the distance of an arbitrary chosen point of the pore space to the closest point of the solid phase is at most r. For system of spherical particles, which we consider here, $H_s(r)$ is a descriptor for the size of the pore size between the spheres [45]. The spherical contact distribution functions of EL-12p, EL-24p, EL-12n and EL-24n are represented in Figure 6 (a). One can observe that the pore space of the samples EL-12p and EL-24p is more fine-structured than the pore space of the samples EL-24n and EL-12n, which corresponds to the larger aggregate particles of n-NCM, see Figure 3. Note that, in general, the particle size distribution does not determine the spherical con-

tact distribution function, which is also influenced by the spatial arrangement of particles, like e.g. clustering or repulsion effects. Note that for H_s, the thickness of the electrode has no influence.

4. Conclusions

In this paper, a characterization of electrode materials is presented combining experiments and statistical image analysis, which gives a detailed insight of electrode quality prepared with different powder materials and processing parameters. In general, values estimated from image data and experimentally measured values are in good accordance with each other. However, it also shows that further valuable information can be obtained by statistical analysis of 3D image data.

Our analysis reveals that the point patterns of particle midpoints, investigated by means of spatial statistics, do not depend on the thickness of the electrode, which is modified during the manufacturing process by the gap height of the doctor blade tool. An interesting result is that a periodic behavior of local volume fractions in dependence of the distance to the foil of the electrode can be observed for cutouts of all electrodes. For both, thin and thick electrodes, this effect averages out, when taking the complete electrode into account for image analysis. Differences between thin and thick electrodes are only visible when computing mean geodesic tortuosity τ and constrictivity β. To be more precise, the shortest path lengths through the thin electrodes are slightly shorter and a stronger effect of bottlenecks can be observed. Since – under the assumption that the additive material is accumulated around the NCM-particles – mean geodesic tortuosity and constrictivity are meaningful characteristics for the effective conductivity of the considered electrodes, the differences in terms of τ and β can result in a different underlying performance of the electrodes during cycling.

Both, experimental methods and statistical image analysis show clearly that there are differences in the electrode porosity and the corresponding transport relevant characteristics for p- and n-type electrodes. Despite of larger particle sizes of the n-NCM powder slightly higher densities or denser packing could be reached compared to p-NCM powder. Besides that, the values of all computed characteristics indicate that the electrodes produced with p-NCM are more fine-structured than the ones produced with n-NCM powder. Nevertheless, the qualitative behavior of the functional characteristics of the point patterns of particle midpoints are rather similar.

The present investigation of electrode materials manufactured under different conditions is a first step towards an approach to tailor the production process such that electrodes with predefined structural properties are obtained. In future work, we intend to complement the present study by additionally investigating the nano-structure of n-NMC particles by means of FIB-SEM tomography.

Acknowledgements

This work has been funded by the German Federal Ministry for Economic Affairs and Energy (BMWi) granted through Project Management Jülich (03ET6095A, 03ET6095B and 03ET6095E).

Data availability

The raw/processed data required to reproduce these findings cannot be shared at this time as the data also forms part of an ongoing study.

References

[1] G. E. Blomgren. The development and future of lithium ion batteries. Journal of The Electrochemical Society, 164(1):A5019–A5025, 2017.

[2] J. F. Peters, M. Baumann, B. Zimmermann, J. Braun, and M. Weil. The environmental impact of Li-ion batteries and the role of key parameters – a review. Renewable and Sustainable Energy Reviews, 67:491–506, 2017.

[3] D. Chen, D. Kramer, and R. Mönig. Chemomechanical fatigue of $LiMn_{1.95}Al_{0.05}O_4$ electrodes for lithium-ion batteries. Electrochimica Acta, 259:939–948, 2018.

[4] A. M. Dreizler, N. Bohn, H. Geßwein, M. Müller, J. R. Binder, N. Wagner, and K. A. Friedrich. Investigation of the influence of nanostructured $LiNi_{0.33}Co_{0.33}Mn_{0.33}O_2$ lithium-ion battery electrodes on performance and aging. Journal of The Electrochemical Society, 165(2):A273–A282, 2018.

[5] Z. Chen, J. Wang, D. Chao, T. Baikie, L. Bai, S. Chen, Y. Zhao, T. C. Sum, J. Lin, and Z. Shen. Hierarchical porous $LiNi_{1/3}Co_{1/3}Mn_{1/3}O_2$ nano-/micro spherical cathode material: minimized cation mixing and improved Li+ mobility for enhanced electrochemical performance. Scientific Reports, 6:25771, 2016.

[6] B. Lin, Z. Wen, Z. Gu, and S. Huang. Morphology and electrochemical performance of $Li[Ni_{1/3}Co_{1/3}Mn_{1/3}]O_2$ cathode material by a slurry spray drying method. Journal of Power Sources, 175(1):564–569, 2008.

[7] L. Li, L. Wang, X. Zhang, M. Xie, F. Wu, and R. Chen. Structural and electrochemical study of hierarchical $LiNi_{1/3}Co_{1/3}Mn_{1/3}O_2$ cathode material for lithium-ion batteries. ACS Applied Materials & Interfaces, 7(39):21939–21947, 2015.

[8] D. L. Wood, J. Li, and C. Daniel. Prospects for reducing the processing cost of lithium ion batteries. Journal of Power Sources, 275:234–242, 2015.

[9] A. Etiemble, N. Besnard, A. Bonnin, J. Adrien, T. Douillard, P. Tran-Van, L. Gautier, Badot, J.-C., E. Maire, and B. Lestriez. Multiscale morphological characterization of process induced heterogeneities in blended positive electrodes for lithium–ion batteries. Journal of Materials Science, 52(7):3576–3596, 2017.

[10] J. Banhart (ed.). Advanced Tomographic Methods in Materials Research and Engineering, volume 66. Oxford University Press, Oxford, 2008.

[11] E. Maire and P. J. Withers. Quantitative X-ray tomography. International Materials Reviews, 59(1):1–43, 2014.

[12] G. Matheron. Random Sets and Integral Geometry. J. Wiley & Sons, New York, 1975.

[13] S. N. Chiu, D. Stoyan, W. S. Kendall, and J. Mecke. Stochastic Geometry and its Applications. J. Wiley & Sons, Chichester, 3rd edition, 2013.

[14] O. Stenzel, O. M. Pecho, L. Holzer, M. Neumann, and V. Schmidt. Predicting effective conductivities based on geometric microstructure characteristics. AIChE Journal, 62:1834–1843, 2016.

[15] K. Kuchler, B. Prifling, D. Schmidt, H. Marköttter, I. Manke, T. Bernthaler, V. Knoblauch, and V. Schmidt. Analysis of the 3D microstructure of experimental cathode films for lithium-ion batteries under increasing compaction. Journal of Microscopy, pages 96–110, 2018.

[16] D. Westhoff, T. Danner, S. Hein, R. Scurtu, L. Kremer, A. Hoffmann, A. Hilger, I. Manke, M. Wohlfahrt-Mehrens, A. Latz, and V. Schmidt. Analysis of microstructural effects in multilayer lithium-ion battery cathodes. Materials Characterization, 151:166–174, 2019.

[17] W. Görner, M. P. Hentschel, B. R. Müller, H. Riesemeier, M. Krumrey, G. Ulm, W. Diete, U. Klein, and R. Frahm. BAMline: the first hard X-ray beamline at BESSY II. Nuclear Instruments and Methods in Physics Research Section A: Accelerators, Spectrometers, Detectors and Associated Equipment, 467–468:703–706, 2001.

[18] L. I. Rudin, S. Osher, and E. Fatemi. Nonlinear total variation based noise removal algorithms. Physica D: Nonlinear Phenomena, 60(1-4):259–268, 1992.

[19] B. A. Dowd, G. H. Campbell, R. B. Marr, V. V. Nagarkar, S. V. Tipnis, L. Axe, and D. P. Siddons. Developments in synchrotron X-ray computed microtomography at the national synchrotron light source. In U. Bonse, editor, Developments in X-ray Tomography II, volume 3772, pages 224–237, 1999.

[20] B. Jähne. Digital Image Processing. Springer, Berlin, 6th edition, 2013.

[21] A. Buades, B. Coll, and J.-M. Morel. A non-local algorithm for image denoising. In IEEE Computer Society Conference on Computer Vision and Pattern Recognition (CVPR 05), volume 2, pages 60–65. IEEE, 2005.

[22] I. Arganda-Carreras, V. Kaynig, C. Rueden, K. W. Eliceiri, J. Schindelin, A. Cardona, and Sebastian S. H. Trainable weka segmentation: a machine learning tool for microscopy pixel classification. Bioinformatics, 33(15):2424–2426, 2017.

[23] I. H. Witten, M. A. Hall, and E. Frank. The WEKA Workbench. Online Appendix for "Data Mining: Practical Machine Learning Tools and Techniques". Morgan Kaufmann, Amsterdam, 4th edition, 2016.

[24] P. Soille. Morphological Image Analysis: Principles and Applications. Springer, New York, 2003.

[25] R. Beare and G. Lehmann. The watershed transform in ITK-discussion and new developments. The Insight Journal, 92:1–24, 2006.

[26] A. Spettl, R. Wimmer, T. Werz, M. Heinze, S. Odenbach, C. E. Krill III, and V. Schmidt. Stochastic 3D modeling of Ostwald ripening at ultra-high volume fractions of the coarsening phase. Modelling and Simulation in Materials Science and Engineering, 23:065001, 2015.

[27] H. Wadell. Volume, shape, and roundness of quartz particles. The Journal of Geology, 43(3):250–280, 1935.

[28] J. Ohser and K. Schladitz. 3D Images of Materials Structures: Processing and Analysis. J. Wiley & Sons, Weinheim, 2009.

[29] B. W. Silverman. Density Estimation for Statistics and Data Analysis. Chapman and Hall, London, 1986.

[30] J. P. K. Seville and C.-Y. Wu. Particle Technology and Engineering: An Engineer's Guide to Particles and Powders: Fundamentals and Computational Approaches. Butterworth-Heinemann, Oxford, 2016.

[31] J. Illian, A. Penttinen, H. Stoyan, and D. Stoyan. Statistical Analysis and Modelling of Spatial Point Patterns. J. Wiley & Sons, Chichester, 2008.

[32] M. Schlather. On the second-order characteristics of marked point processes. Bernoulli, 7(1):99–117, 2001.

[33] K. Lochmann, L. Oger, and D. Stoyan. Statistical analysis of random sphere packings with variable radius distribution. Solid State Sciences, 8(12):1397–1413, 2006.

[34] R. F. Benenati and C. B. Brosilow. Void fraction distribution in beds of spheres. AIChE Journal, 8(3):359–361, 1962.

[35] M. Suzuki, T. Shinmura, K. Iimura, and M. Hirota. Study of the wall effect on particle packing structure using X-ray micro computed tomography. Advanced Powder Technology, 19(2):183–195, 2008.

[36] J. Hoshen and R. Kopelman. Percolation and cluster distribution. I. Cluster multiple labeling technique and critical concentration algorithm. Physical Review B, 14:3438–3445, 1976.

[37] M. B. Clennell. Tortuosity: a guide through the maze. Geological Society, London, Special Publications, 122:299–344, 1997.

[38] L. Holzer, D. Wiedenmann, B. Münch, L. Keller, M. Prestat, P. Gasser, I. Robertson, and B. Grobéty. The influence of constrictivity on the effective transport properties of porous layers in electrolysis and fuel cells. Journal of Materials Science, 48:2934–2952, 2013.

[39] M. Neumann, C. Hirsch, J. Staněk, V. Beneš, and V. Schmidt. Estimation of geodesic tortuosity and constrictivity in stationary random closed sets. Scandinavian Journal of Statistics, in print, 2019, https://doi.org/10.1111/sjos.12375.

[40] M. Neumann, O. Furat, D. Hlushkou, U. Tallarek, L. Holzer, and V. Schmidt. On microstructure-property relationships derived by virtual materials testing with an emphasis on effective conductivity. In M. Baum, G. Brenner, J. Grabowski, T. Hanschke, S. Hartmann, and A. Schöbel, editors, Simulation Science: First International Workshop, SimScience 2017, Göttingen, Germany, April 27-28, 2017, Revised Selected Papers, pages 145–158. Springer, Communications in Computer and Information Science (CIS), Berlin, 2018.

[41] G. Gaiselmann, M. Neumann, O. M. Pecho, T. Hocker, V. Schmidt, and L. Holzer. Quantitative relationships between microstructure and effective transport properties based on virtual materials testing. AIChE Journal, 60(6):1983–1999, 2014.

[42] S. Torquato. Random Heterogeneous Materials: Microstructure and Macroscopic Properties. Springer, New York, 2002.

[43] J. N. Zhou, A. Butera, H. Jiang, and J. A. Barnard. Thickness dependence of the magnetic percolation threshold in as-deposited and annealed $Fe - SiO_2$ granular thin films. Journal of Applied Physics, 84(10):5693–5697, 1998.

[44] S. Stolz, W. Bauer, H.-J. Ritzhaupt-Kleissl, and J. Haußelt. Screen printed electro-conductive ceramics. Journal of the European Ceramic Society, 24(6):1087–1090, 2004.

[45] A. Bezrukov, D. Stoyan, and M. Bargieł. Spatial statistics for simulated packings of spheres. Image Analysis & Stereology, 20(3):203–206, 2011.